

BACHELOR OF ENGINEERING THESIS

---

Observations of Anomalous X-ray  
Pulsar 1E2259+586 with the Rossi  
X-ray Timing Explorer

---

*Author:*

Tim VAN DEN BERG

**THE HAGUE**  
UNIVERSITY  
OF PROFESSIONAL EDUCATION

*Supervisor:*

Lucien KUIPER

**SRON**  
Netherlands Institute for Space Research

May 30, 2013

Tim VAN DEN BERG – *Observations of Anomalous X-ray Pulsar 1E2259+586  
with the Rossi X-ray Timing Explorer* – May 30, 2013

---

## Abstract

---

The observed persistent soft X-ray spectra (0.5 - 10 keV) of anomalous X-ray pulsars (AXPs) can be explained by the magnetar model (Woods and Thompson et al., 2002 [3]) where the emission is powered by the decay of an extreme high magnetic field ( $\geq 10^{14}$  G). Because these spectra are relatively soft, measurements above 10 keV were not expected to detect any hard X-rays. Surprisingly, observations with the Rossi X-ray Timing Explorer (RXTE) and INTEGRAL have shown that AXP sources can have so-called ‘hard spectral tails’ above 20 keV. In this research additional (not used in earlier spectral timing studies) data from RXTE of AXP 1E2259+586 are analyzed in the high-energy range (2 - 250 keV) to confirm or disprove the found indications by Kuiper et al. (2006, [4]) of the same hard spectral tail. In their work they find for other AXPs evidence for pulsed emission above 10 keV and present strong indications for a similar hard spectral tail in 1E2259+586. To obtain the pulse profiles in the high-energy range, timing models of the pulsar’s rotational behaviour have been constructed for the 2 - 4 keV energy band, in which the signal is strong. Analyzing RXTEs Proportional Counter Array (PCA) data from observations performed between October 28, 2003 and December 29, 2011, three different timing models have been constructed to describe the rotational behaviour during this period. The reason for this is the occurrence of two glitches (a star quake with an abrupt change in rotation frequency) at MJD  $54190 \pm 3.5$  d and  $\sim 54881$ . Using these newly derived timing models in the subsequent pulse phase folding analysis for the new observational data yielded again a strong indication (at a  $3.3\sigma$  level) for pulsed emission from 1E2259+586 in the 16.3 - 32.0 keV band. However, a combination of the old and newly analyzed data covering the full RXTE mission period provides no decisive answer to the shape of the pulsed signal above  $\sim 16$  keV. Future observations with more sensitive instruments covering the hard X-ray/soft gamma-ray band like NuSTAR (3 - 80 keV) are required to reach firm conclusions about the existence of a hard spectral tail of 1E2259+586.

---

# Contents

---

<b>Abstract</b>	<b>i</b>
<b>List of Figures</b>	<b>iv</b>
<b>List of Tables</b>	<b>v</b>
<b>List of Abbreviations</b>	<b>vi</b>
<b>1 Introduction</b>	<b>1</b>
1.1 Neutron Stars . . . . .	1
1.1.1 The manifestations of neutron stars . . . . .	2
1.1.2 Magnetars . . . . .	3
1.1.3 Magnetar’s X-ray Spectra . . . . .	4
1.2 1E2259+586 . . . . .	5
1.3 Research Objective . . . . .	5
1.3.1 Approach . . . . .	6
<b>2 Instruments and Observations</b>	<b>7</b>
2.1 Proportional Counter Array . . . . .	8
2.1.1 PCA Operation . . . . .	8
2.2 High Energy X-ray Timing Experiment . . . . .	9
2.2.1 HEXTE Operation . . . . .	10
2.3 Observations . . . . .	10
<b>3 Analysis Methods</b>	<b>13</b>
3.1 Pulse Timing . . . . .	13
3.2 Pulse Profile . . . . .	15
3.2.1 Time of Arrival . . . . .	15
3.3 Timing Solutions . . . . .	16
3.4 Data Screening . . . . .	18

---

3.5 High-energy Pulse Profiles . . . . .	18
<b>4 Results</b>	<b>21</b>
4.1 Timing Solutions . . . . .	21
4.1.1 Pulse Profiles . . . . .	23
<b>5 Summary and Conclusion</b>	<b>29</b>
5.1 Prospects . . . . .	30
<b>A Leap-second</b>	<b>33</b>
<b>B Assignment Description (Dutch)</b>	<b>34</b>
<b>C Uncertainty Timing Models</b>	<b>35</b>

---

## List of Figures

---

1.1	Schematic view of a pulsar . . . . .	2
1.2	Magnetar impression . . . . .	4
2.1	Schematic view RXTE . . . . .	7
2.2	Schematic view PCA . . . . .	8
2.3	Schematic view HEXTE . . . . .	9
3.1	$Z_n^2$ -test distribution around the predicted frequency . . . . .	14
3.2	Pulse profile (histogram) . . . . .	15
3.3	High-statistics template and correlation diagram . . . . .	16
3.4	Phase difference of a set of sub-observations . . . . .	17
4.1	Difference in $\nu$ for timing models A, B and C . . . . .	22
4.2	Pulse profile collage old . . . . .	25
4.3	Pulse profile collage new . . . . .	26
4.4	Pulse profile 16.3 - 34.0 keV . . . . .	27
4.5	Pulse profile collage combined . . . . .	28
A.1	Leap-second . . . . .	33

---

## List of Tables

---

2.1	RXTE Observations of 1E2259+586 . . . . .	11
4.1	1E2259+586 RXTE Ephemerides . . . . .	21
4.2	1E2259+586 Glitches during MJD 52940 - 55925 . . . . .	23

---

## List of Abbreviations

---

<b>ADC</b>	Analog Digital Converter
<b>ASM</b>	All-Sky Monitor
<b>AXP</b>	Anomalous X-ray Pulsar
<b>GTI</b>	Good Time Interval
<b>HEASARC</b>	High Energy Astrophysics Science Archive Research Center
<b>HEXTE</b>	High Energy X-ray Timing Experiment
<b>KDE</b>	Kernel Density Estimation
<b>MJD</b>	Modified Julian Date
<b>NASA</b>	National Aeronautics and Space Administration
<b>PCA</b>	Proportional Counter Array
<b>PHA</b>	Pulse Height Analyzer
<b>PMT</b>	Photomultiplier Tube
<b>RXTE</b>	Rossi X-ray Timing Explorer
<b>SAA</b>	South Atlantic Anomaly
<b>SGR</b>	Soft Gamma-ray Repeater
<b>SNR</b>	Supernova Remnant
<b>TOA</b>	Time Of Arrival

# CHAPTER 1

---

## Introduction

---

”It’s becoming clear that in a sense the cosmos provides the only laboratory where sufficiently extreme conditions are ever achieved to test new ideas on particle physics. The energies in the Big Bang were far higher than we can ever achieve on Earth. So by looking at evidence for the Big Bang, and by studying things like neutron stars, we are in effect learning something about fundamental physics.”

– Sir Martin Rees

To study the physics of compact stellar objects the sources are observed and analyzed in the high-energy range of the electromagnetic spectrum where most of the radiation is emitted. In this research observations in the range of 2 - 250 keV have been performed with the Rossi X-ray Timing Explorer (RXTE) of Anomalous X-ray Pulsar (AXP) 1E2259+586, a fast spinning neutron star within the Supernova Remnant (SNR) G109.1-1.0.

## 1.1 Neutron Stars

Neutron stars are one of the densest objects in the universe, possessing about the same mass as our Sun compressed to a ball of 10 - 30 kilometers across. The material is thought to consist of mainly neutrons what makes them one of the most exotic objects in the sky. Neutron stars can be formed during a supernova explosion of a heavy star where most of its mass is blown away, what is left behind from the core will collapse to form a neutron star. This can

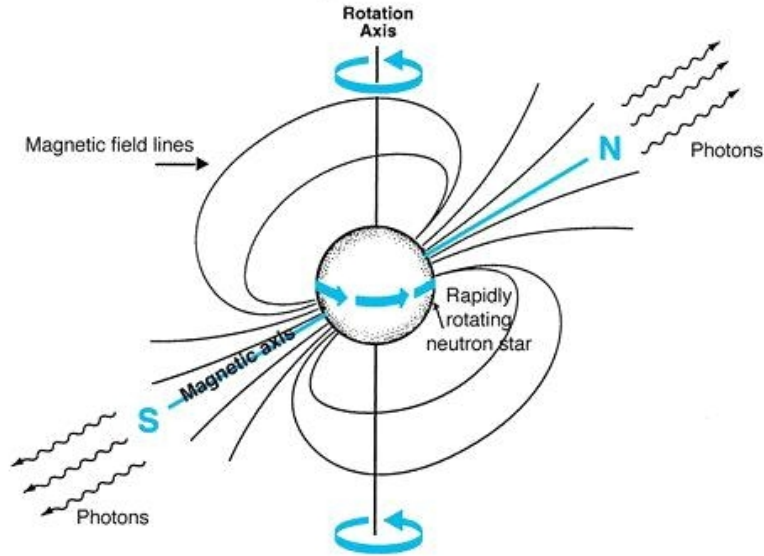


**Figure 1.1:** Schematic view of the rotation powered pulsars geometry [16].

happen if the original star has a mass  $\gtrsim 8 M_{\odot}$  (solar mass;  $1 M_{\odot} \approx 2.0 \cdot 10^{30}$  kg). A different creation scenario is the collapse of a white dwarf star which has accreted matter from a companion star above a critical point ( $\gtrsim 1.4 M_{\odot}$ ). While the outer layers expand, the inner parts of the progenitor star collapse to form a neutron star. Because of the enormous decrease in size in both scenarios, the new star is spinning much faster than the original star due to the conservation of angular momentum [1] [2].

### 1.1.1 The manifestations of neutron stars

Neutron stars manifest differently and emit radiation through various mechanisms. The first and largest class is comprised of the rotation-powered pulsars. In Figure 1.1 a schematic view is presented of the magnetic field configuration of such a system. The fast rotating (observed period range between 2 ms - 10 s) and the high-magnetic field of the order  $10^8 - 10^{13}$  Gauss induce strong voltage gradients in the pulsars magnetosphere, such that particles like electrons and protons can be pulled out from the polar cap region and can subsequently be accelerated near the polar regions to relativistic energies. Along the open field lines the particles escape and form a so-called ‘pulsar wind’. Capable of emitting radiation in the MeV, GeV and TeV range, makes them the highest energy radiating neutron stars. The system (neutron star and its magnetosphere) loses energy and will slow down

because its rotational energy decreases, thus the ultimate source of energy is the rotational energy loss.

Another class consists of the so-called ‘accretion-powered’ pulsars. In this case the neutron star is member of a binary system, through mass transfer from a companion star to the neutron star an accretion disk is formed around the neutron star. The infalling matter can reach very high-temperatures and typically emit in the X-ray range. In this case the gravitational energy released from the infalling matter is the ultimate source that powers these systems.

The last class and most important in this research, is composed of the so-called ‘magnetars’. There are two sub-classes of magnetars which are now understood to be the same: Anomalous X-ray Pulsars and Soft Gamma-ray Repeaters (SGRs). Magnetars emit their energy through the decay of a extreme high (internal) magnetic field ( $\geq 10^{14}$  G). The dissipation of this huge magnetic energy reservoir causes the surface of the neutron star to shine bright in X-rays and cause magnetic field lines to twist, building up severe stresses in the crust near the foot points of the field lines causing glitches (a star-quake, in which the rotation period of the pulsar suddenly changes, much like a Earthquake) and outbursts. This mechanism, providing a luminosity much higher than that of a rotation-powered pulsar is the reason for its ‘anomalous’ classification. Because of anisotropies on the X-ray bright surface and accelerated particles in the magnetosphere the misalignment of the rotation axis and line of sight is the reason for the pulsed nature of these systems. Thompson et al. [3] in 2002 were the first to describe the so-called ‘magnetar model’.

### 1.1.2 Magnetars

The idea of the magnetar model is that after the collapse (during a supernova explosion) a strong magnetic field gets trapped inside the neutron star, when the extreme magnetic field works its way outside the crust the field lines do not align adequately but wrap into a chaotic structure in which the field lines get strangled (shown in Figure 1.2). The magnetic field lines of a young magnetar are continually drifting because of its liquid interior. The continuous internal movement gives rise to enormous (shear) stresses in the compact surface of the star where particles are removed from the surface and inside the star. Electrons accelerated along the strangled field lines, emit their energy through resonant cyclotron scattering. The heated polar regions as an affect of the surface stresses, emit radiation through thermal emission. The stresses can also build up resulting in a glitch or a gamma-ray burst in case of a SGR. The longer the build up period the more energy is released.

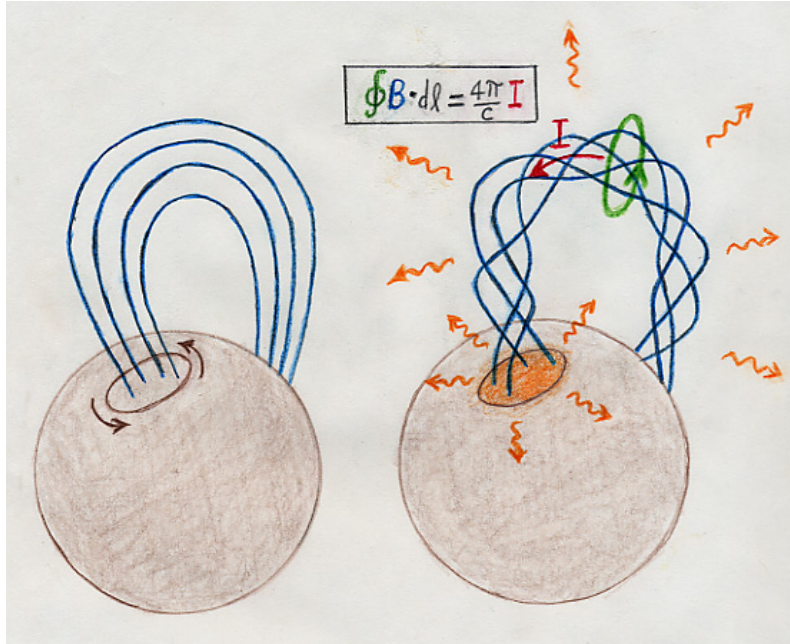


**Figure 1.2:** Impression of the twisted magnetic field lines in a magnetar due to crust motions near the foot points. On the left, situation at start. On the right, the strangled field lines as a result of stresses build up from the foot points to which they are anchored. The formula at the top is Ampere's law, which states a change in the flux of the magnetic field results in a electric current [15].

Whenever stresses occur around the polar regions the magnetic field lines (which are anchored to the surface) get strangled. This situation is shown in Figure 1.2 [3].

### 1.1.3 Magnetar's X-ray Spectra

The X-ray spectra of observed AXPs in the energy range of 0.5 to 10 keV show a mix of thermal and non-thermal components which can best be described phenomenologically by two models: a blackbody and a power-law model. The presence of thermal emission probably requires polar-cap heating, due to the stresses produced from inside the star. The surface temperature of neutron stars are estimated at  $10^5 - 10^6$  K after 1 yr of birth. The non-thermal high-energy emission is most likely the effect of resonant cyclotron scattering by persistent electric currents in the strangled magnetosphere of the neutron star. The mechanism for the so-called 'hard spectral tails' above  $\sim 20$  keV as described in the work of Kuiper et al. (2006, [4]) in the spectrum

of 4 other magnetars, is not yet understood [3].

## 1.2 1E2259+586

Near the center of SNR G109.1-1.0 an X-ray source was found by Gregory and Fahlman (1980) for the first time. Analyzing the source a pulse period of  $\sim 3.489$  s was found, which turned out to be half of the pulse period of  $\sim 6.978$  s due to the almost identical double-peak shaped phase diagram (see Figure 3.2). In 1999 Kaspi et al. [5] obtained for the first time a phase-coherent timing solution for 1E2259+586 with a stability over 2.6 yr. This stability makes a binary interpretation as an accretion-powered pulsar very unlikely. Further observations revealed that the X-ray luminosity was much too high to be powered by the loss of rotational energy (rotation-powered pulsar). This makes 1E2259+586 a solid magnetar member where the emission is powered by the decay of the magnetic field. Furthermore, RXTE observed 80 short X-ray bursts (accompanied by a rotation glitch) of 1E2259+586 with properties that share strong similarities with a SGR. All these phenomena strongly favour a magnetar interpretation [3] [4].

## 1.3 Research Objective

The observed X-ray spectra of AXPs in the energy range of 0.5 - 10 keV can best be described phenomenologically with a blackbody plus a power-law model. Because of the softness of the spectra the model predicted no emission above 10 keV. Only recently (2004) new measurements with the INTEGRAL satellite of AXPs: 1E1841-045, 1RXS J1798-4009, 4U0142-614 and SGRs: SGR-1806-20, SGR-1900+14 have detected (pulsed) hard X-ray and soft gamma-ray emission up to 150 keV. Kuiper et al. [4] were the first to detect the hard spectral X-rays above 10 keV with RXTEs Proportional Counter Array (PCA) and High Energy X-ray Timing Experiment (HEXTE). In earlier observations of 1E2259+586 by Kuiper et al. (2006, [4]) indications were found for a similar hard spectral tail present in the spectra of the other magnetars. In this research additional RXTE observational data collected between October 28, 2003 and December 29, 2011 of AXP 1E2259+586 are analyzed in the energy range of 2 - 250 keV to uncover pulsed hard X-ray emission.

### 1.3.1 Approach

The first part of this research consists of constructing a timing model describing the pulsars rotational behaviour. Because the pulsar loses energy the rotation speed will slow down. This means that the frequency is not constant but will change over time. The models will be constructed from the difference in phase of the obtained phase diagrams for every sub-observation. The phase diagrams are obtained by phase folding each sub-observation around the optimal frequency (Section 3.1 and 3.2). By shifting the obtained phase diagram with respect to a reference diagram (template, see 3.3a) the time shifts are determined (Section 3.2.1) and the time of arrival (TOA) of every sub-observation will be known.

Finally, a timing model can be constructed by fitting the difference in phase of each sub-observation using the method of least squares, to determine the frequency and its time derivatives (the parameters that describe the spin-down rate over time, Section 3.3). The timing models can describe the pulsars rotational behaviour only in case the spin-down behaves smoothly. In case of the occurrence of a glitch, the timing model is only valid for a certain time interval before the glitch, after a glitch a new model with new parameters can be derived to describe the rotational behaviour after. With the timing solutions known the pulse profiles for any high-energy range within the instruments bandwidth can be obtained (in the same way described in Section 3.2) and ultimately looking for the hard pulsed X-ray emission above 10 keV.

## CHAPTER 2

---

### Instruments and Observations

---

Aboard RXTE there are three instruments of which two are important for this study. The first one is the Proportional Counter Array (PCA), for the lower part (2 - 60 keV) of the energy range. The second one is the High-Energy X-ray Timing Experiment (HEXTE), covering the higher energy range (15 - 250 keV). In addition, RXTE carries an All Sky Monitor (ASM). RXTE with its instruments is shown in Figure 2.1 [6].

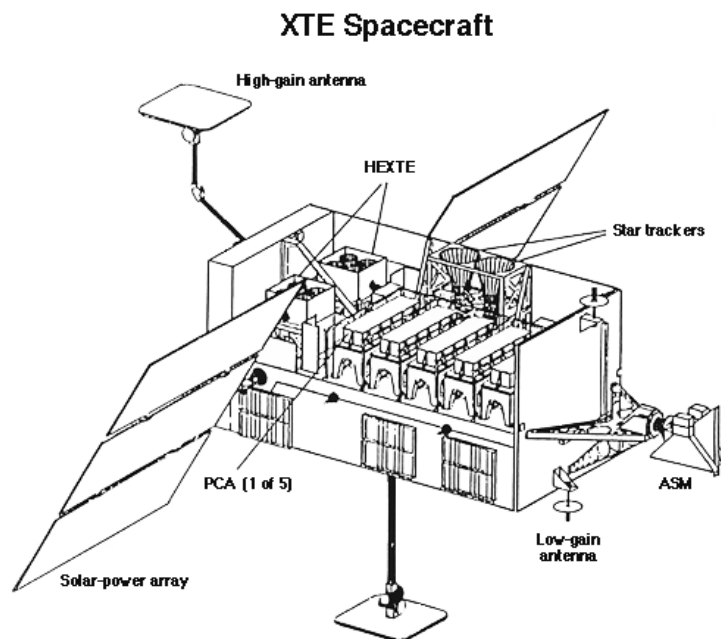


**Figure 2.1:** Schematic see-through view of RXTE [6].

## 2.1 Proportional Counter Array

The PCA carries 5 identical PC-units (PCU) which operate independently. The PCUs are sensitive to X-rays with energies in the range of 2 - 60 keV with a total effective area of 7,000 cm<sup>2</sup> at the peak of the efficiency curve. The PCU can detect the arrival time of each event (incoming photons) with an accuracy of 1  $\mu$ s. Each of the 5 PCUs contain an Analog Digital Converter (ADC) and a 256-channel Pulse Height Analyzer (PHA) to tag each event with an energy value (with a channel width of  $\sim$ 0.25 keV). A schematic view of the PCA is shown in Figure 2.2a [6].

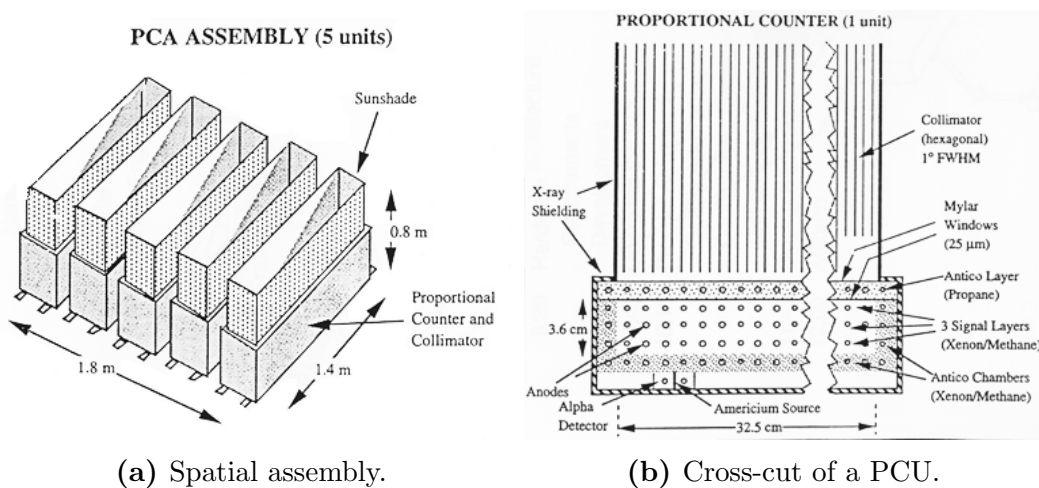


Figure 2.2: Schematic view of the PCA [6].

### 2.1.1 PCA Operation

A proportional counter detector is designed to measure the energy of individual photons. It consists of a collimator and a gas filled chamber (like a geigercounter) that acts as the cathode and a thin wire in the middle as the anode (the five PCU contain three layers with multiple wires, as shown in Figure 2.2b). The chamber is filled with an inert gas, and a quench gas (respectively, xenon and methane in this case) for stabilization.

An incoming photon with enough energy enters the chamber and collides with one of the atoms of the inert gas to produce a free electron and a positive charged ion, known as an 'ion pair'. As the photon travels through the chamber, it leaves a number of ion pairs behind proportional to its energy. Because of the applied electric field the electrons travel to the positively charged anode and the ions to the negative cathode. The applied voltage

in the proportional counter chamber is higher than that of a normal ionization chamber, creating an electric field strength which is large enough to power townsend avalanches (when the electric field is strong enough, the free electron is accelerated to a speed where it can collide with other atoms to produce more ion pairs which themselves repeat the sequence creating the avalanche effect). Because of the geometry of the chamber this happens only fractions of a millimeter from the anode wire to ensure that each multiplication effect is produced by each individual ion pair. A charge amplification up to  $10^6$  can be obtained, greatly improving the signal to noise ratio and therefore reducing the electronic amplification required [7] [9].

## 2.2 High Energy X-ray Timing Experiment

HEXTE consist of two clusters containing each four NaI(Tl)/CsI(Na) scintillation detectors. Each detector has an effective area of  $225 \text{ cm}^2$  and covers the energy range of 15 - 250 keV. HEXTE time tags each incoming photon individually with an accuracy of  $7.6 \mu\text{s}$  (for bright sources 1 ms). The energy of each photon is measured with a PHA. With 256 channels, the photon energy can be determined with an accuracy of  $\sim 1 \text{ keV}$ . A schematic view of HEXTE is shown in Figure 2.3a [6].

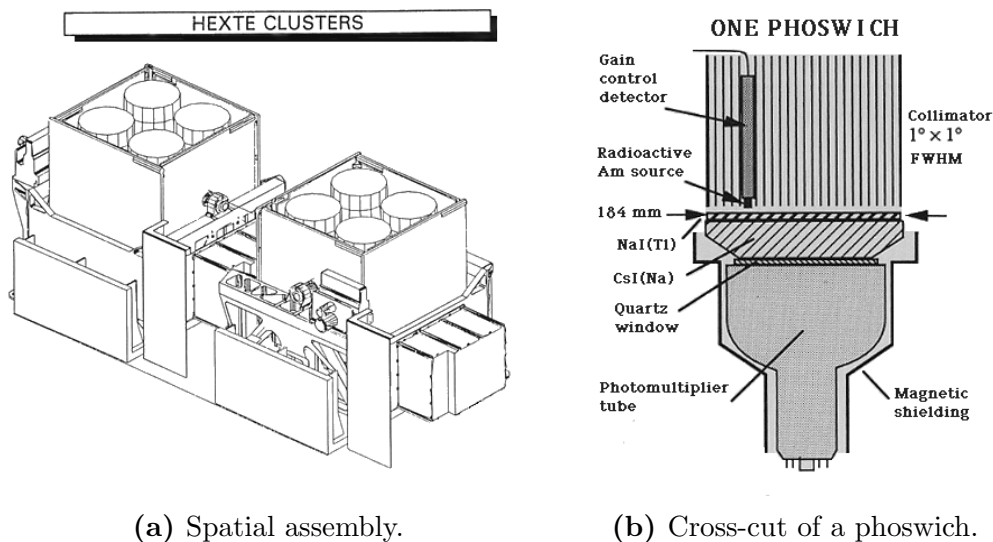


**Figure 2.3:** Schematic view of HEXTE [6].

### 2.2.1 HEXTE Operation

A scintillation detector is designed for the detection of energetic particles and gamma-rays. The detector consist of a collimator, a phoswich (‘phosphor sandwich’, shown in Figure 2.3b) scintillating medium (NaI(Tl)/CsI(Na) crystals), a photomultiplier tube (PMT) and a PHA. The phoswich detector is designed to detect X-rays (and low-energy gamma-rays) with low-intensity in a high-energy background environment. The detector contains a combination of scintillators with different pulse shape characteristics. The primary thin layer of NaI(Tl) is used to absorb the radiation of interest, where as the thicker CsI(Na) layer acts as a anticoincidence layer. By analyzing the pulse shapes, the detector can distinguish the signals and identify in which scintillating crystal the event occurred.

A scintillator consists of a material that absorbs the energy from an incoming particle and re-emits the energy in form of a photon. A PMT is an electron multiplication device with a photocathode (photoelectric emitter) and a number of dynodes (electrodes) with increasing electric potential. When the scintillators are exposed to cosmic radiation, the atoms or molecules are excited and fall back into their ground state while emitting a photon. In the PMT the photon crashes on the photo-cathode which emits a (photo-)electron (photoelectric effect). This electron is accelerated to crash into a dynode, which creates more electrons who are accelerated to the next dynode. This is repeated with enough steps for a measurable signal in the form of a pulse for each individual photon detected. The resulting pulse height produced by the PMT is proportional to the photon intensity emitted by the scintillating medium. Finally, the pulse heights are recorded with a multichannel PHA, that classifies each pulse to a specific energy range [7] [9].

## 2.3 Observations

The data analyzed in this study are taken from observations which begin on the 28th of October, 2003 and end on the 29th of December, 2011. In Table 2.1 the observation cycle identifiers given by the browse tool from NASA’s HEASARC (High Energy Astrophysics Science Archive Research Center) website are shown. The exposure is calculated for the PCU-2 (PCA-unit 2), where the data is screened for Good Time Interval (GTI) exposure time, explained in Section 3.4. Each of the batches labeled as ObsID (Observation Identification) consists of 50 - 70 sub-observations. The exposure time per sub-observation was about 4 ks ( $\sim 1$  hour) on average at observation intervals of 1 week or more. The total of screened PCU-2 exposure analyzed in the

**Table 2.1:** List of RXTE Observations of 1E2259+586 used in this study (PCU-2 screened exposure indicated in last column).

ObsID	Begin Date	End Date	Exposure (ks)
80098	2003 Oct 28	- 2004 Feb 18	33.456
90076	2004 Mar 03	- 2005 Feb 17	103.696
91070	2005 Mar 17	- 2006 Feb 28	214.048
92006	2006 Mar 07	- 2007 Jun 27	271.608
93019	2007 Jul 03	- 2008 Dec 25	309.232
94019	2009 Jan 01	- 2009 Dec 30	195.416
95019	2010 Jan 07	- 2010 Dec 30	216.416
96019	2011 Jan 13	- 2011 Dec 29	207.856
			1,551.728

study amounts  $\sim 1.55$  Ms ( $\sim 2.6$  Weeks of continuous exposure).



# CHAPTER 3

---

## Analysis Methods

---

In this chapter the analysis methods used in this work are described, providing the determination of the optimal instantaneous frequency, the pulse profile, the time of arrivals (TOAs), a phase coherent timing solution, data screening and the pulse phase event distributions as a function of energy.

### 3.1 Pulse Timing

The pulse timing of 1E2259+586 is done with the PCA in the energy range of 2 - 4 keV where the pulsed signal is strongest. In previous observations, a pulsed signal at a rate of  $\sim 0.14329$  Hz was detected. Because the PCUs mostly collect background events e.g. photons from other sources, special mathematical techniques are used to extract the underlying pulsed emission in the field of view. In this study a  $Z_n^2$ -test (Buccheri et al., 1983 [10]) search in a small window around the predicted frequency is done. The window size is typically 2.5 independent Fourier steps, with  $\Delta\nu_{IFS} = 1/\tau$ , in which  $\tau$  represents the time lapse of the sub-observation (search number is 25 steps of  $0.1 \Delta\nu_{IFS}$ ). The pulse phase of an event (photon) is calculated from Equation 3.1 [8].

$$\phi_i = \phi_0 + \nu(t_i - t_0) + \frac{1}{2}\dot{\nu}(t_i - t_0)^2 + \frac{1}{6}\ddot{\nu}(t_i - t_0)^3 \quad (3.1)$$

where

$\phi_0$	pulse phase at $t_0$	[-]
$\phi_i$	pulse phase at $t_i$	[-]
$\nu$	(predicted) frequency	[Hz]

$\dot{\nu}$	frequency derivative	[Hz/s]
$\ddot{\nu}$	frequency second derivative	[Hz/s <sup>2</sup> ]
$t_i$	barycentered photon arrival time	[s]
$t_0$	barycentered epoch of timing model	[s]

Where  $i$  represents the photon (event) index. Note that the  $\nu$  changes for the chosen steps around the predicted frequency. The parameters  $\dot{\nu}$  and  $\ddot{\nu}$  are hold fixed at values from ephemerides used in earlier analysis of 1E2259+586 by Kuiper et al [4] and takes into account possible small phase drifts over the sub-time interval. Mostly, we can set these values safely to zero given the observation duration of typically an hour. The phase values are used to evaluate the statistical variable  $Z_n^2$ , to calculate the optimal frequency with Equation 3.2 [10].

$$Z_n^2 = (2/N) \sum_{k=1}^n \left[ \left( \sum_{i=1}^N \cos k\phi_i \right)^2 + \left( \sum_{i=1}^N \sin k\phi_i \right)^2 \right] \quad (3.2)$$

where

$Z_n^2$	statistical parameter	[-]
$n$	chosen number of harmonics	[-]
$N$	number of events (photons detected)	[-]

Because of the double-peak shaped signal (see e.g. the pulse profile in 2 - 4 keV band shown in Figure 3.3a) 2 harmonics ( $n = 2$ ) are used in the evaluation of  $Z_n^2$ . In Figure 3.1 the result of Equation 3.2 is shown for frequencies in the trial frequency window (25 scan steps of size  $0.1 \Delta\nu_{IFS}$ ).

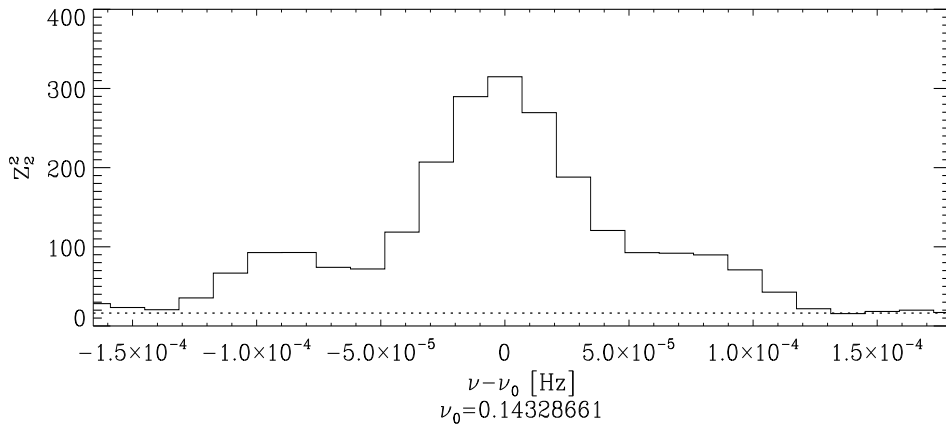


**Figure 3.1:** Distribution around the predicted frequency for one of the observations, as obtained with a  $Z_2^2$ -test (Equation 3.2).

## 3.2 Pulse Profile

With the optimal frequency found in the search, the pulse profile in the 2 - 4 keV band can be obtained by phase folding the photon arrival times. This is done by trimming the phases of the events to residuals in the 0 - 1 range by subtracting its integer part (signal is repetitive). The collected events from the pulsar are sorted accordingly in phase bins to form a phase diagram. In Figure 3.2 an example of a phase diagram is shown for a certain sub-observation. The measured (histogram) profile is superposed with a so-called Kernel Density Estimation (KDE; a smooth representation of a underlying genuine pulse shape, used only for visualization purposes) and its  $1\sigma$  deviation (marked with dotted lines). The uncertainty of every count/bin is calculated with  $\sqrt{n}$ , where  $n$  is the number of counts per bin. For bin number 10 in Figure 3.2, the uncertainty is marked with a vertical line (at  $\phi \sim 0.52$ ).

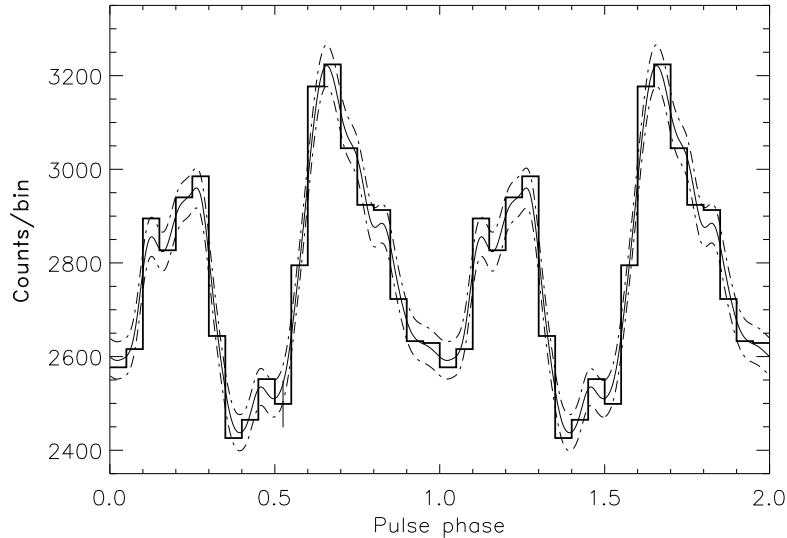


**Figure 3.2:** Pulse profile (histogram) of a certain sub-observation in the 2 - 4 keV band with a KDE shape and its  $1\sigma$  deviation. Two cycles are shown for clarity.

### 3.2.1 Time of Arrival

To determine the TOA for each sub-observation, the pulse phase distribution from the folding process applying the optimal frequency (Figure 3.2) is cross

correlated with a high-statistics template (see Kuiper et al. [4], shown in Figure 3.3a). The global maximum of the correlation diagram (Figure 3.3b; in this example near shift  $\Delta\phi_{max} \sim 0.87$ ) determines the time shift of size  $\Delta\phi_{max}/\nu$  (i.e. the phase shift between both diagrams) to be applied to a chosen time-zero point (mid-time of sub-observation) to align it with the template [8].

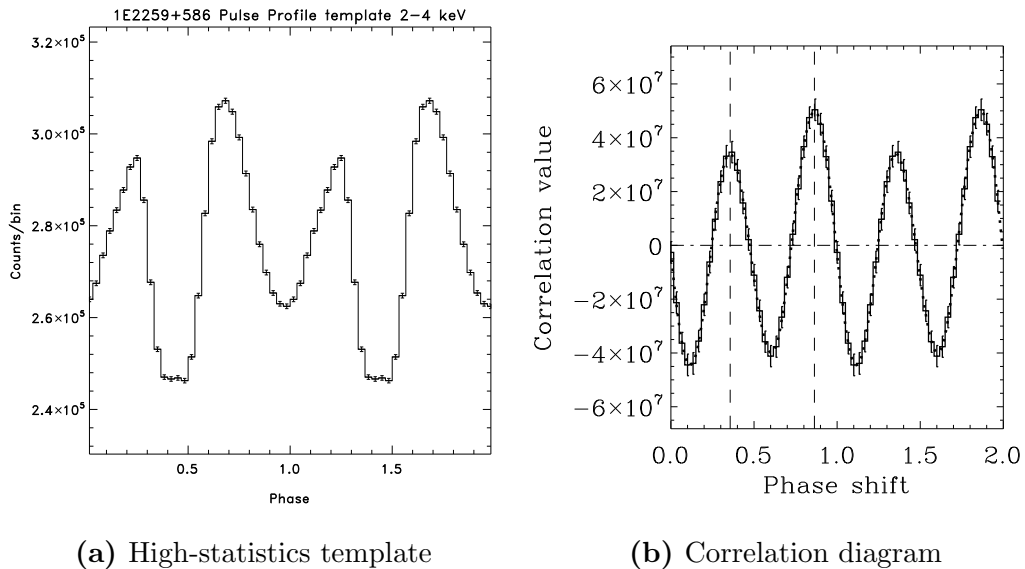


**Figure 3.3:** Left: High-statistics 2 - 4 keV template used in the correlation procedure based on the work of Kuiper et al. [4]. Right: Correlation diagram from which the phase shift can be obtained. Two cycles shown for clarity.

### 3.3 Timing Solutions

All the assembled TOAs are folded upon a trial timing solution to obtain the phase residuals. The parameters  $\nu = \frac{d\phi}{dt}$ ,  $\dot{\nu} = \frac{d^2\phi}{dt^2}$  and  $\ddot{\nu} = \frac{d^3\phi}{dt^3}$  from Equation 3.1, can be determined by fitting the pulse arrival time phase residuals with a standard  $\chi^2$  minimization technique (method of least squares) as described by Kuiper et al. [8]. In this method the increments of  $\nu$ ,  $\dot{\nu}$  and  $\ddot{\nu}$  which minimize the  $\chi^2$  statistics can be determined from Equation 3.3 to obtain a so-called ‘phase-coherent’ timing solution describing adequately every revolution of the neutron star.

$$\Delta\phi_i = \nu_{inc}(t_p - t_0) + \frac{1}{2}\dot{\nu}_{inc}(t_p - t_0)^2 + \frac{1}{6}\ddot{\nu}_{inc}(t_p - t_0)^3 \quad (3.3)$$

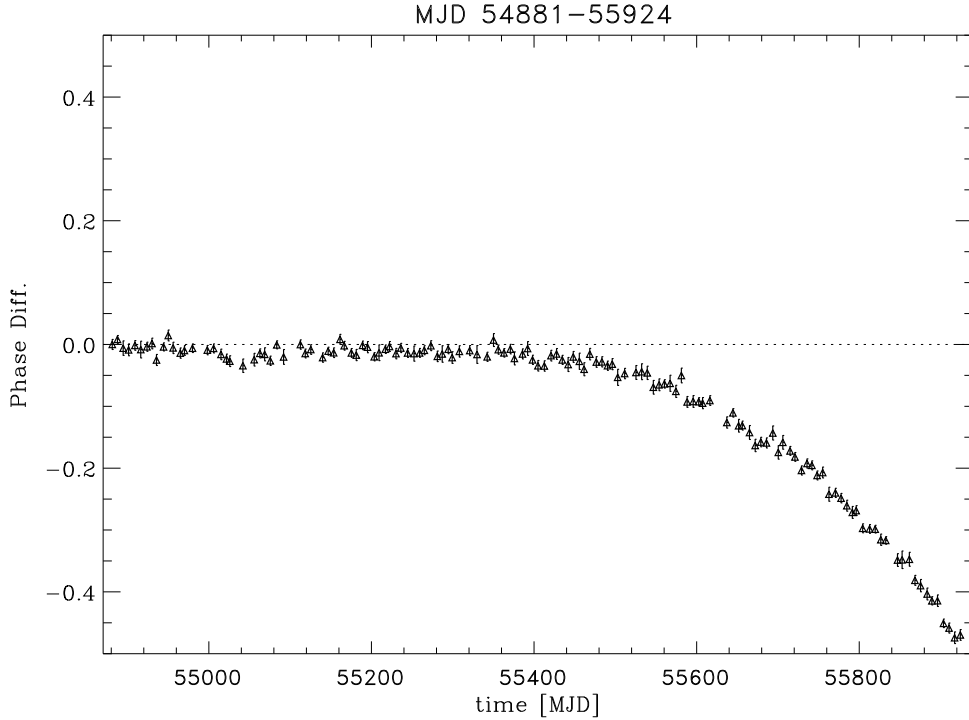


**Figure 3.4:** The phases of every TOA folded upon a trial timing model constituting  $\nu_{trial}$ ,  $\dot{\nu}_{trial}$  and  $\ddot{\nu}_{trial}$  (shown as triangular shaped data points). The timing solution is valid up to approximately halfway the graph. After Modified Julian Date (MJD)  $\sim 55400$  the model fails to describe the rotational behaviour properly. A new solution can be obtained with Equation 3.3 to minimize the scatter around 0.0 by optimizing  $\nu_{inc}$ ,  $\dot{\nu}_{inc}$  and  $\ddot{\nu}_{inc}$  simultaneously.

Where  $t_p$  is the TOA of the pulse in each sub-observation. In Figure 3.4 the phase differences are shown for a certain set of sub-observations. The optimum timing parameters ( $\nu = \nu_{trial} + \nu_{inc}$ ,  $\dot{\nu} = \dot{\nu}_{trial} + \dot{\nu}_{inc}$  and  $\ddot{\nu} = \ddot{\nu}_{trial} + \ddot{\nu}_{inc}$ ) can be obtained over a time interval of sub-observations where the spin-down can be described by a smooth algebraic function in terms of a Taylor series expansion of  $\nu(t)$  [8].

In case of a glitch the timing solution is only valid for a certain time interval before, after this discontinuity a new solution must be found with updated new timing parameters to describe the rotational behaviour after [11].

### 3.4 Data Screening

With the timing model(s) known for the observation period shown in Table 2.1, the 'raw' data are subjected to a so-called 'good time interval' (GTI)- A and B screening process.

In part A the occasionally occurring 'break-down' periods of certain PCA units during an observation are removed from the data set. In case of the PCA this is done for all 5 units. The PCA detector break-down is a typical 'aging' problem of the detectors, in course of operations these phenomenon occurred more and more frequently. For the PCA the average number of PCUs in use at the start in 1996 was five, during the end in 2012 this number was two.

Part B of the screening process consists of 4 elements. The first element is the determination of the proper start and end time of the observation. Observation programs include many objects all over the sky, when switching between, the so-called 'slew' data is removed. In our case the data collection is accepted once the angle between target and actual satellite pointing is smaller than  $3'$  to ensure a stable pointing.

The second element is the interference of Earth and its atmosphere (itself a strong X-ray/gamma-ray source). Data collecting is only accepted when the source is  $5^\circ$  above the Earth's limb to avoid background radiation from the Earth's atmosphere and to ensure source visibility.

The third reason for unusable data is the time of passage through the South Atlantic Anomaly (SAA). The SAA is a region of the Earth's magnetosphere in which the radiation of energetic charged particles is strongly enhanced. During passage through the SAA the instruments saturate by the high particle flux and these periods should therefore be avoided.

The last selection criterion is the number of events collected by a particle counter to monitor the local background environment [6].

### 3.5 High-energy Pulse Profiles

Once the GTI intervals are known and the proper timing models (ephemerides) are available to accurately describe the rotational behaviour of the AXP, the pulse profiles for any energy range within the instruments bandwidth can be obtained. With the PHA every event collected by the PCA and HEXTE is classified in one of the 265 channels. The events are phase folded with the same technique as described in Section 3.1, sorted accordingly to their PHA channel (measured energy equivalent) and pulse phase values. The pulse

profiles are obtained in the energy ranges like the ones shown by Kuiper et al. [4] (see also Figure 4.2).



# CHAPTER 4

---

## Results

---

In this chapter the results of the timing analysis and pulse profiles of 1E2259+586 resulting from the pulse phase folding are shown.

### 4.1 Timing Solutions

To describe the rotational behaviour of 1E2259+586 for the observation periods given in Table 2.1, three different timing solutions turned out to be necessary. Particularly, two glitches have been detected during this period. The results of the method to create phase coherent timing models described in Section 3.3, are shown in Table 4.1. All three timing solutions were obtained by fitting the pulse phase residuals of the arrival times of each sub-observation with the method of least squares. For every solution three timing parameters,  $\nu$ ,  $\dot{\nu}$  and  $\ddot{\nu}$  were necessary to describe the rotational behaviour of the AXP for the given epochs.

**Table 4.1:** 1E2259+586 RXTE Ephemerides. Uncertainties are given for a 68% confidence level ( $=1\sigma$ ).

Timing-solution	$t$ (MJD)	$t_0$ (MJD)	$\nu$ (Hz)	$\dot{\nu}$ ( $10^{-15}$ Hz/s)	$\ddot{\nu}$ ( $10^{-24}$ Hz/s <sup>2</sup> )
A	52940 - 54187	52940	0.14328707260(1)	-9.995(5)	2.9(1)
B	54194 - 54881	54194	0.14328612331(3)	-10.15(2)	7.4(8)
C	54881 - 55925	54881	0.14328552183(2)	-9.635(9)	-0.9(2)

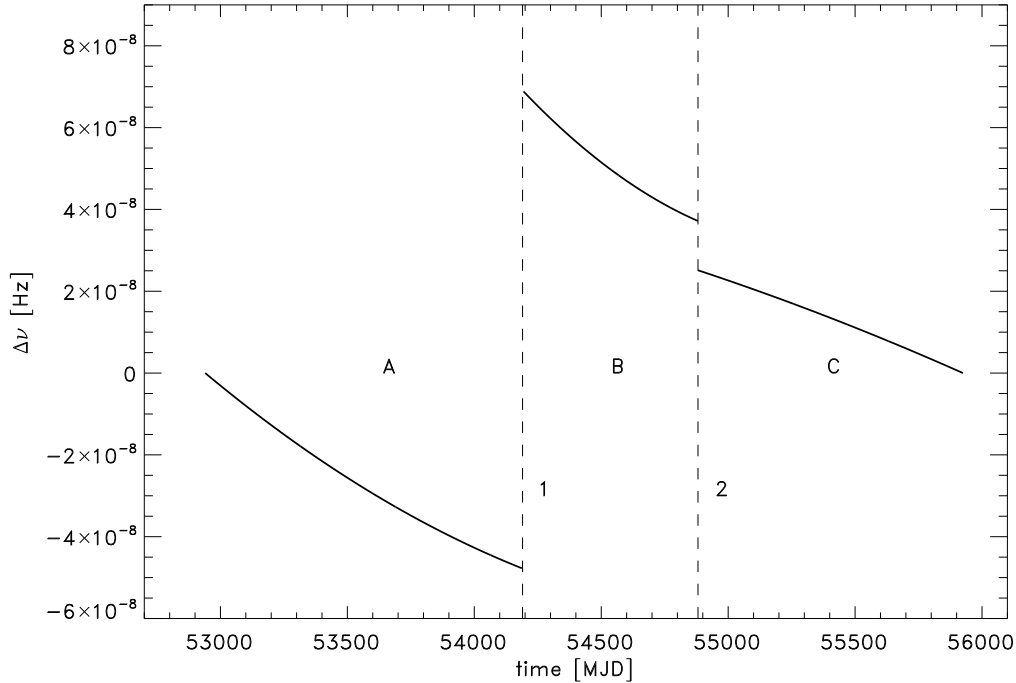


**Figure 4.1:** Difference in  $\nu$  during MJD 52940 - 55925 with indicated timing models A, B and C, and glitches 1 and 2 (marked with dotted lines). The frequency difference shown along the y-axis has been obtained by subtraction a linear frequency model (= straight line) valid from  $t_{start}$  to  $t_{end}$  (values  $\nu_{start}$  and  $\nu_{end}$ ) from the actual reconstructed frequency values using the timing models (see Table 4.1) for visualization purposes.

In Figure 4.1 the three timing models and the two glitches the pulsar endured are labeled with A, B and C, and glitches 1 en 2, respectively. The first spin-up glitch occurred at MJD  $54190 \pm 3.5$  d, and second spin-down (micro-)glitch near MJD  $\sim 54881$ . In Table 4.2 the jumps in  $\nu$ ,  $\dot{\nu}$  and fractional jumps ( $\Delta\nu/\nu$ ,  $\Delta\dot{\nu}/\dot{\nu}$ ) for both glitches are shown (note the difference in signs of  $\Delta\dot{\nu}$ , indicating a slope change during glitch 1 and 2, visible in Figure 4.1). The uncertainties in the numbers are calculated with the partial derivatives of Equation C.1, shown in Appendix C. Glitch 2 we find, coincides with one glitch reported in the work of İcđem et al. (2012, [12]). They find a micro-glitch at MJD  $\sim 54880$  with  $\Delta\nu = -2.00(15) \cdot 10^{-9}$  and  $\Delta\dot{\nu} = 2.91(22) \cdot 10^{-16}$ , which is inconsistent with our findings. They also claim a micro-glitch at MJD  $\sim 53750$ . In the analysis done in this research an anomalous phase difference in our phase residuals was found in the sub-

**Table 4.2:** 1E2259+586 Glitches during MJD 52940 - 55925

Glitch	$t$ (MJD)	$\Delta\nu$ (Hz)	$\Delta\dot{\nu}$ (Hz/s)	$\Delta\nu/\nu$ (-)	$\Delta\dot{\nu}/\dot{\nu}$ (-)
1	$\sim 54190.5$	$1.192(9)\cdot 10^{-7}$	$-4.7(2)\cdot 10^{-16}$	$8.319(1)\cdot 10^{-7}$	$4.7(2)\cdot 10^{-2}$
2	$\sim 54881$	$-1.2(2)\cdot 10^{-8}$	$0.8(5)\cdot 10^{-16}$	$-0.8(2)\cdot 10^{-9}$	$-0.8(5)\cdot 10^{-2}$

observation around MJD  $\sim 53750$ . This was a consequence of an improper implementation of a leap-second correction (a one-second time adjustment, see Appendix A) in the RXTE PCA instrument software, and not a microglitch. During MJD  $\sim 54000$  -  $54250$  they find no phase connection, where as our derived models A, B and glitch 1 have no trouble describing the rotational behaviour.

### 4.1.1 Pulse Profiles

With the timing solutions derived for the newly analyzed observation period MJD 52940 - 55925, the pulse-profiles from PCA/HEXTE can be obtained for any chosen energy range within the instruments bandwidth. Because of morphology changes in the pulse profiles with increasing energy, we show the profiles for the narrow energy bands. In Figure 4.2 the result of the work by Kuiper et al. [4] based on RXTE observations of 1E2259+586 from September 29, 1996 to October 28, 2003 are shown. In their work they find with the PCA pulsed emission above 10 keV with a 10.6, 5.2 and 3.1  $\sigma$  deviation from an uniform distribution in the energy range of respectively 8.3-11.9, 11.9-16.3 and 16.3-24.0 keV (profiles  $c-e$ ). The HEXTE sensitivity is too low to detect any underlying pulsed emission above  $\sim 15$  keV (profile  $f$ ). The total amount of screened exposure time (PCU-2) for their observations in total was  $\sim 700$  ks, while in this new study about a double of exposure time has been added ( $\sim 1.550$  ks, see Table 2.1) [4].

The results of the data analysis in this research are shown in Figure 4.3. Profiles  $c-f$  (above 10 keV) show significant deviations with respectively 8.3, 2.3, 1.5 and  $\sim 2\sigma$  indicating pulsed emission above  $\sim 10$  keV. It is interesting to note that the newly obtained profiles above 10 keV are less significant than those shown earlier by Kuiper et al. [4], while we doubled the exposure time. However, we still have strong indications for pulsed emission above  $\sim 16$  keV, where the 16.3 - 32.0 keV profile presented in Figure 4.4) shows a  $3.3\sigma$  deviation from uniformity, strengthening the earlier indications by Kuiper et al. [4]. Also note the morphology changes in the double-peaked profiles below 10 keV, especially the pronounced existence of a narrow pulse-

like feature in the deepest minimum (clearest visible in profile *b* in Figure 4.2 and 4.3).

The combined observations from Kuiper et al. [4] and the new data analyzed in this research are shown in Figure 4.5. With a total of  $\sim 2.200$  ks exposure time, a 13.5, 5.4, 2.8 and  $\sim 2\sigma$  deviation from uniformity is obtained in the energy ranges of respectively 8.3-11.9, 11.9-16.3, 16.3-24.0 and 14.8-27.0 keV (Figure 4.5*e – f*).

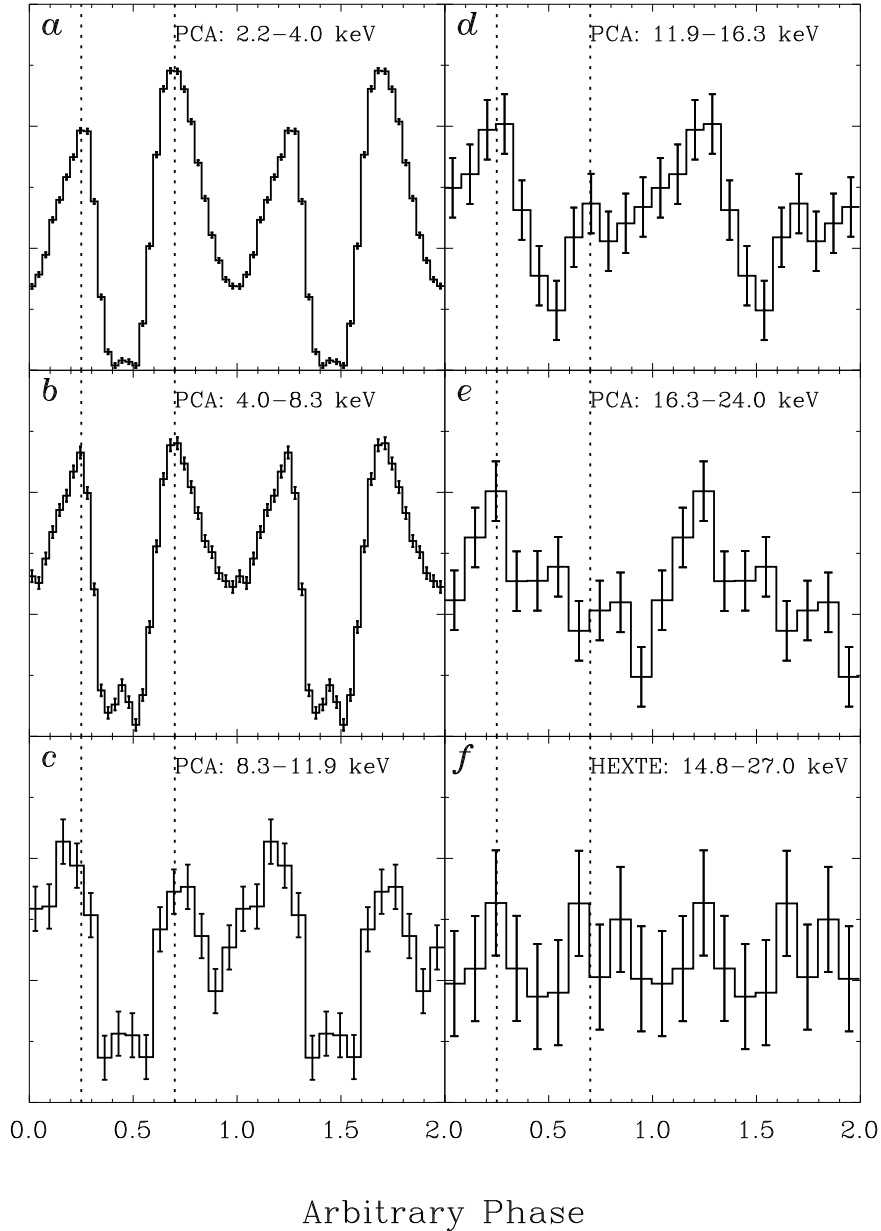


**Figure 4.2:** Pulse profiles of 1E2259+586 in the energy range 2.2 - 27.0 keV from combined observations (September 29, 1996 to October 28, 2003) with PCA/HEXTE. Two cycles are shown for clarity. The vertical dotted lines serve as a guide for alignment comparison [4].

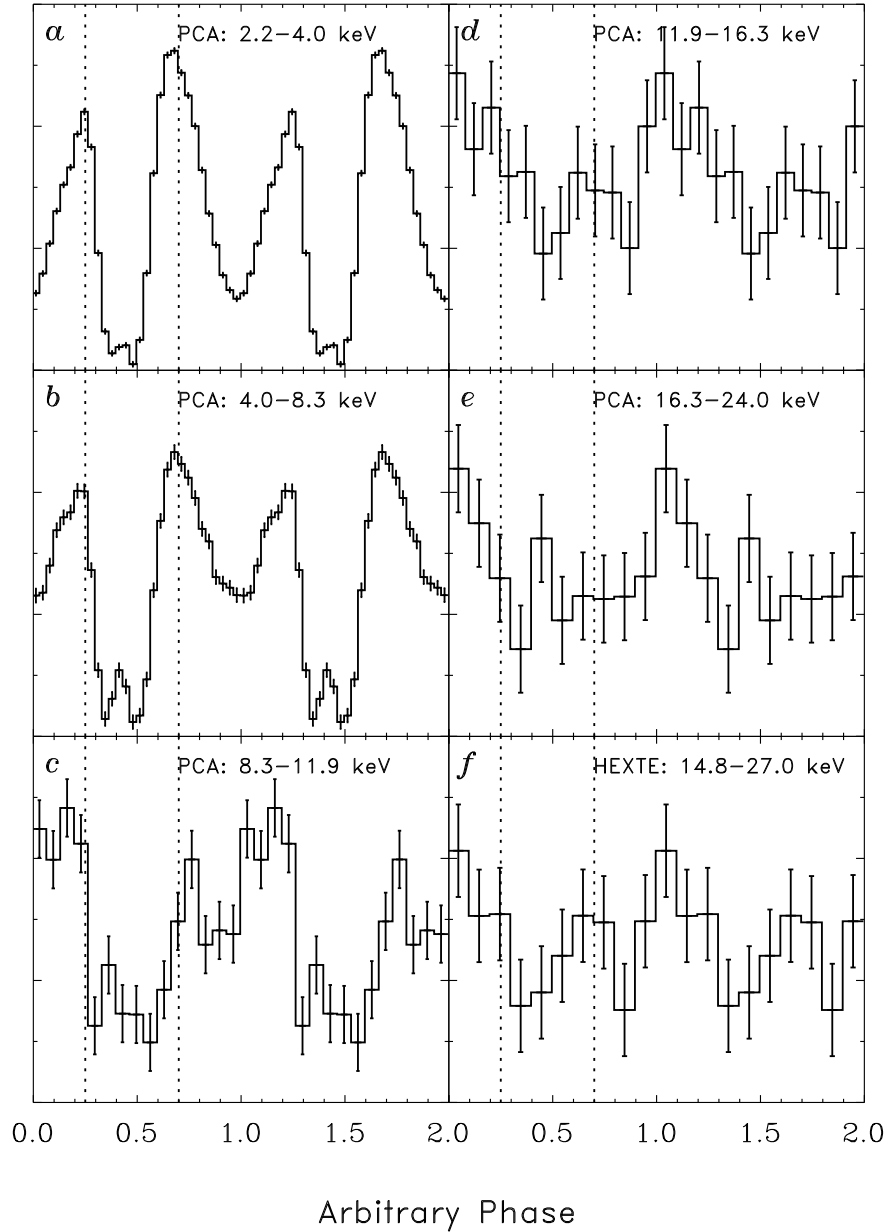


**Figure 4.3:** Pulse profiles of 1E2259+586 in the energy range 2.2 - 27.0 keV from the combined new observations (October 29, 2003 to December 31, 2011) with PCA/HEXTE. Two cycles are shown for clarity. The vertical dotted lines serve as a guide for alignment comparison.

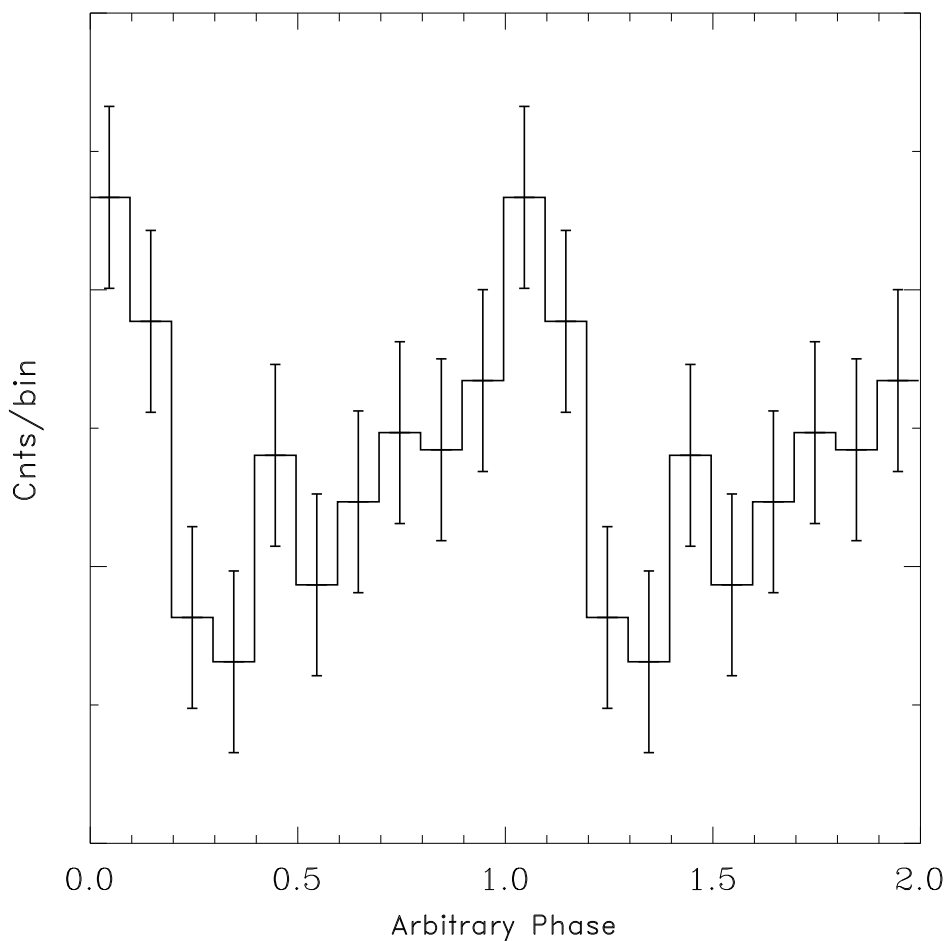


**Figure 4.4:** PCA pulse profile of 1E2259+586 in the energy range 16.3 - 32.0 keV showing a  $3.3\sigma$  deviation from uniformity thus strengthening the indications for pulsed emission above  $\geq 16$  keV by Kuiper et al. [4] (analyzing the new combined observations between Oct 28, 2003 and Dec 31, 2011).

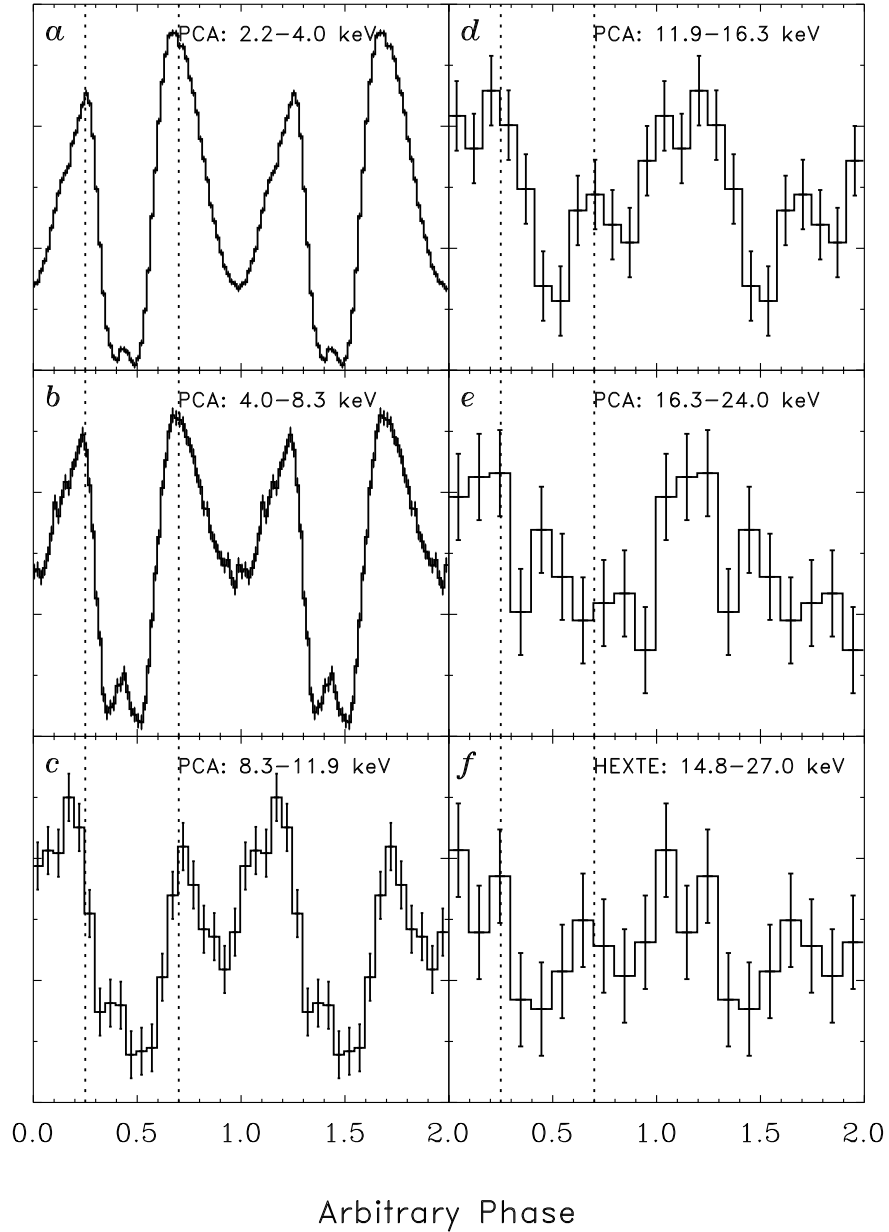


**Figure 4.5:** Pulse profiles of 1E2259+586 in the energy range 2.2 - 27.0 keV from the combined new observations (Figure 4.3) plus the data provided by Kuiper et al. (Figure 4.2) with PCA/HEXTE. Two cycles are shown for clarity. The vertical dotted lines serve as a guide for alignment comparison.

## CHAPTER 5

---

### Summary and Conclusion

---

In this work additional RXTE PCA/HEXTE data have been analyzed from RXTE observations performed between the 28th of October, 2003 and the 29th of December, 2011. A total of  $\sim 1.5$  Ms of additional screened exposure of 1E2259+586 have been collected with the PCA unit-2 detector, more than twice the exposure time collected before Oct 28, 2003 (see Kuiper et al. [4]). A timing analysis of the PCA data from observations covering this period showed that three simple timing models are required to satisfactorily describe the rotational behaviour of 1E2259+586, for we detected two rotation glitches in this period: one regular spin-up glitch at  $\text{MJD } 54190 \pm 3.5 \text{ d}$  (March 31, 2007) and an anti-glitch at  $\text{MJD } \sim 54881$  (February 19, 2009). Equipped with these newly obtained timing models we phase-folded all screened RXTE PCA and HEXTE data from the Oct. 28, 2003 - Dec. 31, 2011 period to obtain pulse profiles from any energy band in the instruments bandwidth. We found again a strong indication ( $3.3\sigma$ ) for pulsed emission in the 16.3 - 32.0 keV band, supporting the earlier indications (Kuiper et al. [4]). However, combining all RXTE observations of 1E2259+586 (2.2 Ms of PCU-2 exposure) the  $\gtrsim 16.3$  keV signal weakens to about a  $2\sigma$  deviation indicating possible shifts in the lightcurve structure as a function of time, or is simply related to the very low signal to noise at these particular energies. In conclusion, in spite the huge observation time collected during the mission lifetime of about 2.2 Ms the RXTE PCA is not sensitive enough to give a decisive answer on the presence of hard pulsed emission and the existence of a hard tail for AXP 1E2259+586. Observations with much more sensitive instruments covering the hard X-ray band ( $\geq 10$  keV) like those aboard NuSTAR (or ASTRO-H) are required to reach final conclusions on the presence

of a hard spectral tail in 1E2259+586.

## 5.1 Prospects

Analyzing the full RXTE PCA/HEXTE data of AXP 1E2259+586 collected over the whole RXTE mission lifetime of more than 16 years (Dec. 30, 1995 - Jan. 5, 2012), resulting in a 2.2 Ms of PCU-2 exposure, we could not reach decisive answers on the existence of hard pulsed emission above  $\sim 16$  keV and on the presence of a hard tail. Apparently, in spite the huge exposure time the sensitivity of RXTE PCA and HEXTE is insufficient to securely detect the hard high-energy component of 1E2259+586. The Nuclear Spectroscopic Telescope Array Mission (NuSTAR) launched on June 13, 2012 is the first focussing telescope in the hard X-ray band (3 - 80 keV) and about a factor of 10 - 100 more sensitive than RXTE. 1E2259+586 is included in NuSTAR's observation program and in the period of April 24 - 27, 2013 a total of 123 ks of exposure time was collected on this AXP. A presentation by Honjun An during the workshop "The Fast and Furious", hold in Madrid on May 22 - 24, 2013 on "NuSTAR results and future plans for magnetars and rotation-powered pulsars" showed that analyzing the first 55 ks of 1E2259+586 exposure a clear 20 - 50 keV signal from imaging analysis was present in the NuSTAR data, providing the existence of a hard tail for 1E2259+586 for which we had strong indications. We eagerly wait now for further results from this mission on 1E2259+586.

---

## Bibliography

---

- [1] Philip A. Charles, Frederick D. Seward – *Exploring the X-ray Universe. Section 3.6: Remnants with neutron stars*, Cambridge University Press, 1995
- [2] Victoria M. Kaspi and Mallory S. E. Roberts – *Isolated Neutron Stars*, 2006
- [3] Woods P.M., Thompson C. – *Soft Gamma-ray Repeaters and Anomalous X-ray Pulsars: Magnetar Candidates*, 2006
- [4] Kuiper L. et al. – *Discovery of luminous pulsed hard X-ray emission from anomalous X-ray pulsars 1RXS J1708-4009, 4U 01242+61 and 1E2259+586 by INTEGRAL and RXTE*, 2006
- [5] Kaspi V.M. et al. – *Precision Timing of Two Anomalous X-Ray Pulsars*, 1999
- [6] Technical Appendix to the XTE NRA – *The RXTE Technical Appendix (Appendix F)*, 1995
- [7] Glenn F. Knoll – *Radiation Detection and Measurement*, 4th Edition, J. Wiley and Sons, 2010
- [8] Kuiper L, Hermsen W. et al. – *High-energy characteristics of the schizophrenic pulsar PSR J1846 in Kes 75*, 2006
- [9] Safa O. Kasap – *Optoelectronics and Photonics: Principles and Practices. Chapter 5: Detectors*– Prentice Hall, 2001
- [10] Buccheri R. et al. – *Search for pulsed  $\gamma$ -ray emission from radio pulsars in the COS-B data*, 1983
- [11] Donald W. Marquardt – *An Algorithm for Least-Squares Estimation of Nonlinear Parameters*, 1963

- [12] İçdem B. et al. – *RXTE timing analysis of the anomalous X-ray pulsar 1E2259+586*, 2012
- [13] Helmut Kopka, Patrick W. Daly – *Guide to Latex, Tools and Techniques for Computing Typesetting*, Fourth Edition, 2004
- [14] Gumley, Liam E. – *Practical IDL programming, creating effective data analysis and visualization applications*, 2002
- [15] Robert C. Duncan – ‘*Magnetars*’, *soft gamma-ray repeaters and very strong magnetic fields*, 2003
- [16] [http://www.visualphotos.com/image/1x6017381/rotating\\_neutron\\_star\\_pulsar\\_diagram](http://www.visualphotos.com/image/1x6017381/rotating_neutron_star_pulsar_diagram)

# APPENDIX A

---

## Leap-second

---

The anomalous phase difference of  $\sim -0.128(5)$  visible at MJD  $\sim 53750$  in Figure A.1 (corresponding to  $\Delta t = \Delta\phi \cdot P \approx -0.128(5) \cdot 6.97885 = -0.894 \pm 0.035$  s), as a result of a improper implementation of a leap-second.

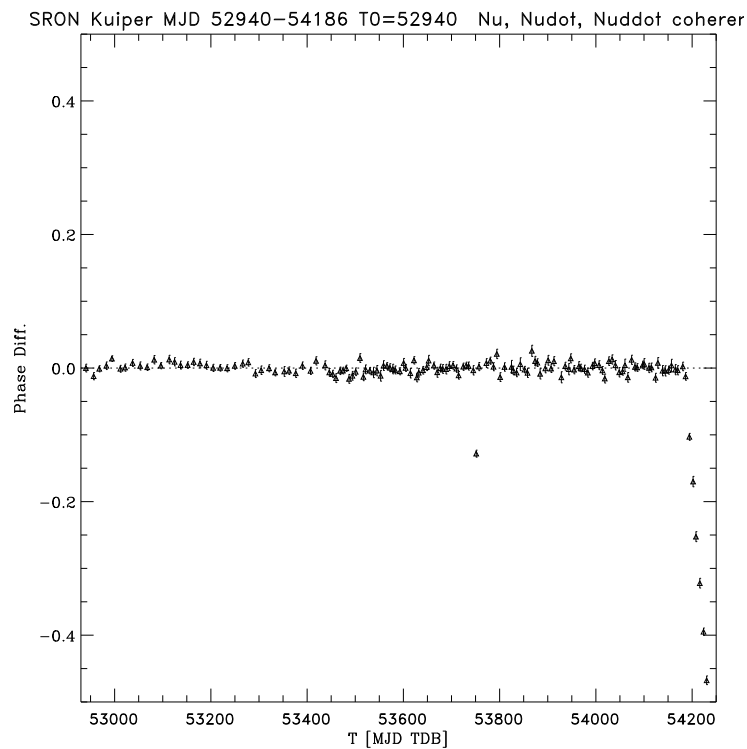


**Figure A.1:** Phase difference of a set of sub-observations.

## APPENDIX B

---

### Assignment Description (Dutch)

---

Betreft : Stage plan stagiair Tim van den Berg

Periode : Feb. 4 - Mei 31, 2013

Begeleider SRON: Dr. L. Kuiper

Titel project : "Confirming the hard spectral tail in AXP 1E2259+586 using RXTE PCA/HEXTE data"

Het stage werk dat Tim zal verrichten bestaat uit het construeren van tijdsmodellen voor "anomalous" X-ray pulsar 1E2259+586 uit RXTE PCA waarnemingen, die genomen zijn na 28 October 2003 tot het einde van de RXTE missie (begin Januari 2012). Gebruikmakend van deze modellen worden de RXTE PCA en HEXTE data "gevouwen" om de beste pulse profielen te verkrijgen als functie van energie. Hieruit zal Tim het gepulste spectrum bepalen voor energien tussen de 3 en 150 keV. We hopen hiermee een ONAFHANKELIJKE bevestiging te krijgen voor het bestaan van een harde ( $>10$  keV) spectrale staart in 1E2259+586, waarvoor we sterke aanwijzingen hebben uit eerdere RXTE data, genomen voor 28 October 2003. Door de combinatie van ALLE RXTE PCA/HEXTE data kunnen we de aller beste spectrale informatie verkrijgen voor het gepulste spectrum van 1E2259+586. Een bevestiging zou de 4-de detectie betekenen van een "persistente" AXP met een harde spectrale staart. Het generen van de tijdsmodellen vergt ongeveer 2/3 maanden tijd, terwijl het gepulste spectrum in een maand bepaald kan worden, de laatste maand zal besteed worden aan het op papier zetten van het gedane werk in de vorm van een scriptie.

## APPENDIX C

---

### Uncertainty Timing Models

---

The uncertainty values given for the glitches (jumps in  $\nu$  and  $\dot{\nu}$ ) presented in Table 4.2, are calculated with the partial derivatives of Equation C.1 where the uncertainty in  $\nu$  for a given time (occurrence of the glitch in this case) can be calculated. For both glitches this is done using the ephemerides (see Table 4.1) before and after the glitch. Finally, by adding both  $\sigma_\nu^2$  values calculated with Equation C.3 and taking the square root of that number, the uncertainty in the glitch is calculated.

$$\nu = \nu_0 + \dot{\nu}(t - t_0) + \frac{1}{2}\ddot{\nu}(t - t_0)^2 \quad (\text{C.1})$$

Where  $t$  is the time of interest (glitch) and  $t_0$  the reference time for which the timing parameters are calculated (shown in Table 4.1). The partial derivatives of Equation C.1 are shown below in Equation C.2.

$$\sigma_\nu^2 \approx \left( \left( \frac{\partial \nu}{\partial \nu_0} \right) \Delta \nu_0 \right)^2 + \left( \left( \frac{\partial \nu}{\partial \dot{\nu}} \right) \Delta \dot{\nu} \right)^2 + \left( \left( \frac{\partial \nu}{\partial \ddot{\nu}} \right) \Delta \ddot{\nu} \right)^2 \quad (\text{C.2})$$

What results in Equation C.3.

$$\sigma_\nu^2 \approx \Delta \nu_0^2 + (t - t_0)^2 \Delta \dot{\nu}^2 + \left( \frac{1}{2}(t - t_0)^2 \right)^2 \Delta \ddot{\nu}^2 \quad (\text{C.3})$$

For the uncertainty in timing parameter  $\dot{\nu}$  the same technique is applied.